Journal of Alloys and Compounds 731 (2018) 723–730

Contents lists available at ScienceDirect

Journal of Alloys and Compounds

journal homepage: http://www.elsevier.com/locate/jalcom

Improving the thermoelectric properties of $SrTiO_3$-based ceramics with metallic inclusions

Deepanshu Srivastava [a], Colin Norman [a], Feridoon Azough [a], Marion C. Schäfer [b], Emmanuel Guilmeau [b], Robert Freer [a, *]

[a] School of Materials, University of Manchester, Manchester, M13 9PL, UK
[b] Laboratoire CRISMAT, UMR 6508 CNRS/ENSICAEN, 6 bld Maréchal Juin, 14050, Caen Cedex, France

ARTICLE INFO

Article history:
Received 6 July 2017
Received in revised form
4 October 2017
Accepted 5 October 2017
Available online 6 October 2017

Keywords:
Perovskite
Thermoelectric
Inclusions
Oxide
Grain boundary

ABSTRACT

High quality $Sr_{0.8}La_{0.067}Ti_{0.8}Nb_{0.2}O_{3-\delta}$ ceramics containing inclusions of Cu or Fe were prepared by the mixed oxide route and sintered under reducing conditions at 1700 K. Products were high density; Fe enhanced density (to 98% theoretical) and grain size (to 15 μm) whilst Cu tended to reduce both slightly. XRD and SEM analyses showed that the material is mainly composed of cubic $SrTiO_3$ phase, with rutile-structured minor phases and metallic inclusions along the grain boundaries. The inclusions increased carrier concentration and carrier mobility, leading to a reduction in electrical resistivity by a factor of 5 and increase in power factor by 75%. Both types of metallic inclusions were beneficial, increasing the thermoelectric figure of merit (ZT) from 0.25 at 1000 K for the control sample, to ZT of 0.36 at 900 K for the Cu-containing samples and to 0.38 at 1000 K for the Fe-containing samples.

1. Introduction

A range of potential applications for thermoelectric materials has been developed in recent decades. Not only have they been widely applied in niche applications such as radioisotope thermoelectric generators (RTGs), but plentiful prototypes for energy scavenging/harvesting, sensing and wearable devices have been developed as a result of extensive studies on these materials [1]. Oxides have been considered as promising materials since the demonstration of the thermoelectric properties of Na_xCoO_2 [2]. Oxides offer advantages over conventional materials on the basis of superior chemical and thermal stability [3].

Thermoelectric efficiency is dependent on the difference between the source and sink temperatures. Physical properties of the thermoelectric material affect the figure of merit, ZT which is given by Ref. [1]:

$$ZT = \left(\frac{S^2\sigma}{\kappa}\right)T \quad (1)$$

where, S is the Seebeck coefficient, σ is the electrical conductivity and κ is the thermal conductivity and T is the mean operating temperature.

The requirement for high ZT, n-type material at temperatures over 600 K has driven research on oxides such as $SrCrO_3$, $CaMnO_3$, ZnO, In_2O_3 and $SrTiO_3$ [4]. Strontium titanate (STO) is a leading candidate and the undoped material has a large Seebeck coefficient ~ 850 μVK^{-1}, but low electrical conductivity and high thermal conductivity. There have been many approaches to improve the properties of $SrTiO_3$. A single crystal of La doped $SrTiO_3$ has been reported to have a similar power factor ($S^2\sigma$) to that of Bi_2Te_3 at room temperature (2800–3600 $\mu W/K^2m$) [5]. However the high thermal conductivity of undoped $SrTiO_3$, in the range 6–12 W/mK, from room temperature to 1000 K [6], remains an important factor limiting the improvement of overall ZT. The thermoelectric performance of the STO based ceramics has been addressed by simultaneously improving the power factor and introducing phonon scattering centres to reduce the thermal conductivity. The difficulty in this approach is further accentuated by the increased electronic component of thermal conductivity as the electrical resistivity is reduced (parameters being linked by the Wiedmann-Franz law [7]). Dehkordi et al. [8,9] have shown significant improvement in power factor of STO by using Pr doping and optimizing the presence of Pr-rich inclusions at grain

* Corresponding author.
E-mail address: Robert.Freer@manchester.ac.uk (R. Freer).

https://doi.org/10.1016/j.jallcom.2017.10.033

boundaries using non-equilibrium heating rates. The main factors that improve the properties are the influence of donor-type oxygen vacancies in bulk compositions and of cationic substitution. Doped $SrTiO_3$ prepared under reducing conditions has been particularly promising with ZT values as large as 0.41 at 1073 K being obtained [10]. Other work has demonstrated that A and B site doping and variation of processing conditions can enhance the thermoelectric properties of these perovskites [11–16]. Co-doping on the A/B sites and doping with heavy elements (in particular Dy [10,16] and W [15]) have been effective in reducing thermal conductivity by phonon scattering. In addition, the generation of oxygen vacancies, by processing the materials under reducing conditions, has been equally beneficial for STO, leading to the creation of additional charge carriers as the oxidation states of transition elements (particularly Ti/Nb) are adjusted [6,14,17–19]. The control of A-site cationic vacancies is also gaining attention as a route to improve thermoelectric properties. Popuri et al. [20] have demonstrated temperature independent thermal conductivity for STO where 27% A-sites are vacant. Related work has explored the effect of A-site vacancies generated by a range of co-dopants [19–23]. Notably, Lu et al. [22] also investigated vacancy ordering as the defect concentration is increased and its subsequent effect on crystal structure and thermoelectric properties; a maximum ZT of 0.41 at 1000 K was obtained for material containing 10–20% A-site vacancies. In the present work, we have investigated an optimized composition of $Sr_{0.8}La_{0.06}Ti_{0.8}Nb_{0.2}O_3$, which has 13.3% A-site vacancies, while processing under reducing conditions to create oxygen deficiency.

The addition of conductive second phases can also improve the electrical conductivity by reducing grain boundary resistance. Previous work has included the addition of graphene at concentrations less than the percolation level as a means to enhance electrical conductivity [24]. In the case of $Sr_{0.9}La_{0.1}TiO_3$, the addition of 15% silver as a second phase was shown to increase the ZT through an increase in the electrical conductivity and a decrease in the thermal conductivity [25]. The latter was associated with increased phonon scattering at the second phase grain boundaries. Zheng et al. [26] prepared $Sr_{0.9}La_{0.1}TiO_3$ ceramics containing up to 15% Ag in the matrix by hydrothermal synthesis and reported significant improvement in electrical conductivity and modest improvement in the Seebeck coefficient. There was also a reduction in thermal conductivity, but that may have been related to density and microstructure changes. Additions of silver have also been employed to improve the electrical and thermal properties of $Ca_3Co_4O_9$. Wang et al. [27], and Mikami et al. [28] added silver both as a second phase and as a dopant; the latter was more effective in reducing thermal conductivity with the Ag acting as a phonon scatterer in the lattice. In $BaTiO_3$ ceramics the addition of silver has been shown to improve the strength and electrical properties [29,30]. However, in some materials the presence of silver may cause problems. For example, Iwagami et al. [31] found that the use of silver as an electrode for $Bi_{1/2}Na_{1/2}O_3$ ceramics led to rapid diffusion along grain boundaries causing the properties to degrade. The low melting point of silver (1235 K) tends to promote diffusion during sintering, making microstructural control more difficult. The use of other metallic inclusions may overcome the limitations of silver. Qin et al. [32] investigated the effect of including up to 20 wt % metallic Ti particles in $SrTiO_3$. They found that metallic Ti is not a very effective additive as it results in formation of non-stoichiometric TiO_{2-x} and properties that depend sensitively on sintering conditions.

The candidate metallic inclusions chosen for this study were iron and copper, having melting points of 1811 K and 1358 K respectively. The melting temperature of iron is above that used for sintering strontium titanate whilst copper has a melting temperature below the sintering temperature [19,23,24]. The doping of $SrTiO_3$ by Fe and Cu has previously been studied for application in magnetic fields [33], photocatalysis [34] and oxygen sensors [35]. However, in these cases the metals were introduced as dopants within the structure of the perovskite lattice and not as separate inclusions. The presence of iron within the strontium titanate lattice has been shown to significantly increase the conductivity especially near the strontium ferrite end of the phase diagram [36]. However, because of the presence of high concentrations of oxygen vacancies the conduction is ionic [37]. The solubility of copper in $SrTiO_3$ is limited and any excess is present as CuO [38,39] which can be readily reduced to Cu. These additives are relatively cheap compared to Ag, have high electrical conductivity compared to many other prospective metal additives and moderate electronegative values, which allows their oxides to be easily reduced to the metallic state under reducing sintering conditions.

2. Experimental

The starting powders were: $SrCO_3$ (Sigma Aldrich, UK); La_2O_3 (Molycorp Inc, USA); Nb_2O_5 (Solvay, UK); TiO_2 (Sachtleben Chemie GmbH); all had >99.9% purity. They were mixed in the appropriate molar ratios to produce the base formulation $Sr_{0.8}La_{0.06}Ti_{0.8}Nb_{0.2}O_3$, denoted as L2. The mixed powders were milled for 24 h with yttria-stabilized zirconia balls and propan-2-ol in a weight ratio of 1:1:1. The homogeneous slurry was dried overnight and then calcined in air at 1425 K. These mixing and calcination stages were repeated.

Metal nitrate solutions of $Fe(NO_3)_3 \cdot 9H_2O$ and $(Cu(H_2O)_6](NO_3)_2)$ were individually mixed with batches of L2 powder to give an additional 2.5 wt% of Fe or Cu. The powders were mixed homogeneously using the incipient wetness technique, which exploits capillary forces [40]. The appropriate volumes and concentrations of the solutions needed for incipient wetness were determined prior to mixing. The powders were dried in an oven at 350 K and then heated in air at 750 K to decompose the starting nitrates to their corresponding oxides. The powders were then milled using an agate mortar and pestle and pressed uniaxially in a hardened steel die to produce cylindrical pellets 20 mm diameter and 5 mm thick. The pellets were sintered in a Vecstar tube furnace (model No. VTF7 SP) at 1700 K for 24 h under 1 bar total pressure, with reducing atmosphere of Ar-5% H_2.

The densities of the sintered ceramics were determined using the Archimedes method. Circular cross-sections of individual specimens were cut using a diamond wheel, then ground and polished down to a 1 μm diamond paste followed by silica solution (OPS) ready for phase and microstructural analysis. X-ray diffraction (XRD) was carried out using a Philips X'pert diffractometer with Cu source; the 2θ scan angle was 10°–85° with step of size 0.030° and a dwell time of 10 s at each step. The XRD spectra were refined using the Rietveld program Topas [41].

Scanning electron microscopy (SEM) was undertaken on a Phillips XL30 FEGSEM equipped with a Rontec EDX, energy dispersive spectroscopy system. The samples were polished using OPS solution to obtain mirror like finish. Grain sizes were determined by the linear intercept method. Electron Backscatter Diffraction (EBSD) analysis was undertaken on a Quanta 85 650-FEGSEM microscope, equipped with an Oxford Instruments EBSD detector (Nordlys II).

X-ray photoelectron spectroscopy (XPS) was carried out using a Kratos Axis Ultra instrument with a monochromated Al Kα X-ray source. Samples were polished cross-sections. Detailed scans of electronic transitions of core levels were performed with a resolution of 0.05 eV; data were collected for areas of 700 × 300 μm. Charge compensation was performed for all samples and peak fitting was carried out using CASAXPS software. The carbon 1*s* peak

at 284.8 eV was used for calibration purposes. Background subtraction from acquired data was carried out using the Shirley approximation. All the characteristic peaks were fitted using the GL30 peak shape which is a mixture of Gaussian plus 30% Lorentzian.

The electrical resistivity (ρ) and Seebeck coefficient (S) of the bulk samples were determined from 300 K to 1050 K using a ZEM-III (Ulvac-Riko) under a helium atmosphere. Samples were typically 10 mm × 3 mm × 3 mm in size. Charge carrier concentrations were determined by use of a Physical Property Measurement System (Quantum Design-PPMS) at 300 K. The specimens were typically 2.5 mm × 2.5 mm x 0.3 mm in size. Thermal diffusivity was determined from 300 K to 1100 K using an in-house laser flash facility [42]. The Cowan method [43] was used to model the compensation in heat loss and obtain temperature-dependant thermal diffusivity. Specific heat capacity was determined by differential scanning calorimetry (Netzsch STA 449 C).

3. Results and discussion

After sintering at 1700 K under reducing conditions, all the samples were of high density. Samples prepared without metallic additions, as baseline reference, were of 95.5% theoretical density, whilst the Cu-containing samples were marginally lower at 93.8%, and Fe-containing samples slightly higher at 98.2% theoretical density.

The conversion of the starting powders into the desired $SrTiO_3$-based phase and metallic particles is confirmed by X-Ray diffraction spectra (Fig. 1); the primary phase has the perovskite cubic structure with space group symmetry *Pm-3m*. Peaks for the secondary phase $Ti_xNb_{1-x}O_y$ are visible in the spectrum. Evolution of this rutile based structure has been demonstrated in A-site deficient formulations [19]. The presence of metallic Fe and Cu in the 'added' samples is confirmed in Fig. 1. From Topas refinement, the lattice parameters of the strontium titanate phase increased from 3.923 Å in the L2 control sample to 3.928 Å and 3.931 Å for samples prepared with Fe and Cu metal additions respectively. It is inferred that some of the Fe and Cu diffused into the strontium titanate primary matrix increasing the lattice parameter. With a high solubility at the B-site, Fe and Cu ions can be readily accommodated within the lattice, increasing the lattice parameter [33,38,44]. Rietveld refinement of the X-ray diffraction spectra suggested that the metallic phases represent approximately 2.0% of the sample; this is marginally less than the amount added to the starting powder, but within the uncertainty level of the analysis. The Ar-5% H_2 atmosphere used for sintering was essential to reduce the Fe/Cu oxides to the corresponding metallic inclusions and was also beneficial in reducing Ti in the matrix to enhance thermoelectric properties [19].

Fig. 2 shows typical micrographs of the three types of samples. The microstructure of the control sample (Fig. 2a) showed the presence of two phases together with porosity, mainly at grain boundaries. The grey phase is the perovskite matrix and frequently the grains exhibit lighter coloured core regions. This is due to variation in the composition of the grains with the centres being La and Nb rich [19]. The darker phase, predominately found at grain boundaries, is the rutile-structured $Ti_xNb_{1-x}O_y$, identified in the X-ray diffraction spectra (Fig. 1). Both the Fe- and Cu-containing samples (Fig. 2b and c) have similar microstructures to the control sample but in addition exhibit a much brighter phase at the grain boundaries and triple point junctions. EDS analysis confirmed these to be the Cu or Fe rich inclusions. Some of the metallic phases were located near voids, indicating the possible presence of a liquid phase and high diffusion gradients of metallic inclusions that could impede sintering. The size of these inclusions was in the range of 1–3 μm. Any sub-micron inclusions were difficult to differentiate at grain boundaries. However, they were observable using EBSD, as shown in Fig. 3.

In the control samples the grain sizes were typically 10 μm (Fig. 2a), but only 7 μm–10 μm for samples prepared with Cu additions (Fig. 2c) and larger at 15 μm for samples prepared with Fe additions (Fig. 2b). These values probably reflect differences in diffusion rates and contrasting melting temperatures of Fe and Cu (1811 K and 1358 K respectively). It is clear that the presence of the solid iron particles did not inhibit grain growth. Rheinheimer et al. [45] demonstrated the existence of wetting surfaces and their impact on grain growth rates in $SrTiO_3$. They showed that wetting was associated with titania-based second phases located at grain boundaries, and reported exaggerated grain growth, in the presence of wet boundaries, when samples were sintered under reducing environments at temperatures near 1733 K. This is in agreement with our observations of much higher grain growth rates in samples prepared with Fe additives. Sintering at 1700 K, which is close to the melting temperature of iron, will lead to the development of partially wetted grain surfaces along the grain boundaries which will enhance grain growth. In contrast for Cu additives, the melting temperature of copper is much lower, which

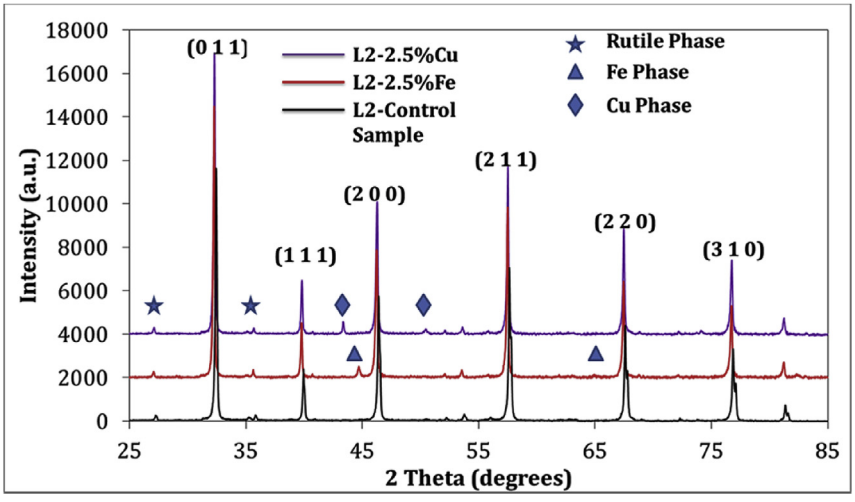

Fig. 1. X-ray diffraction spectra for the $Sr_{0.8}La_{0.06}Ti_{0.8}Nb_{0.2}O_3$ samples (L2) prepared with and without metallic additions.

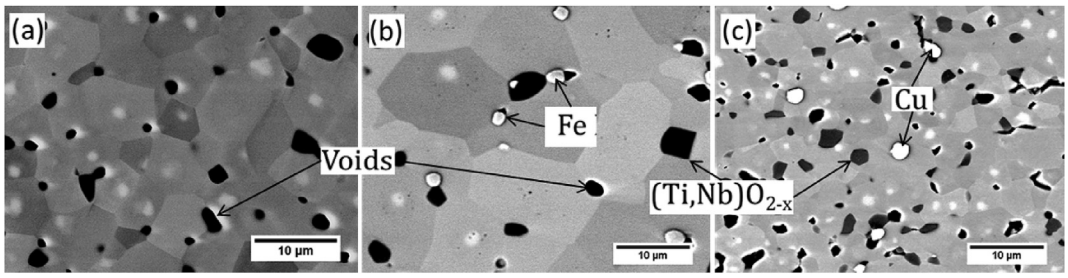

Fig. 2. SEM micrographs of $Sr_{0.8}La_{0.06}Ti_{0.8}Nb_{0.2}O_3$ samples: (a) control, (b) prepared with Fe additions, (c) prepared with Cu additions.

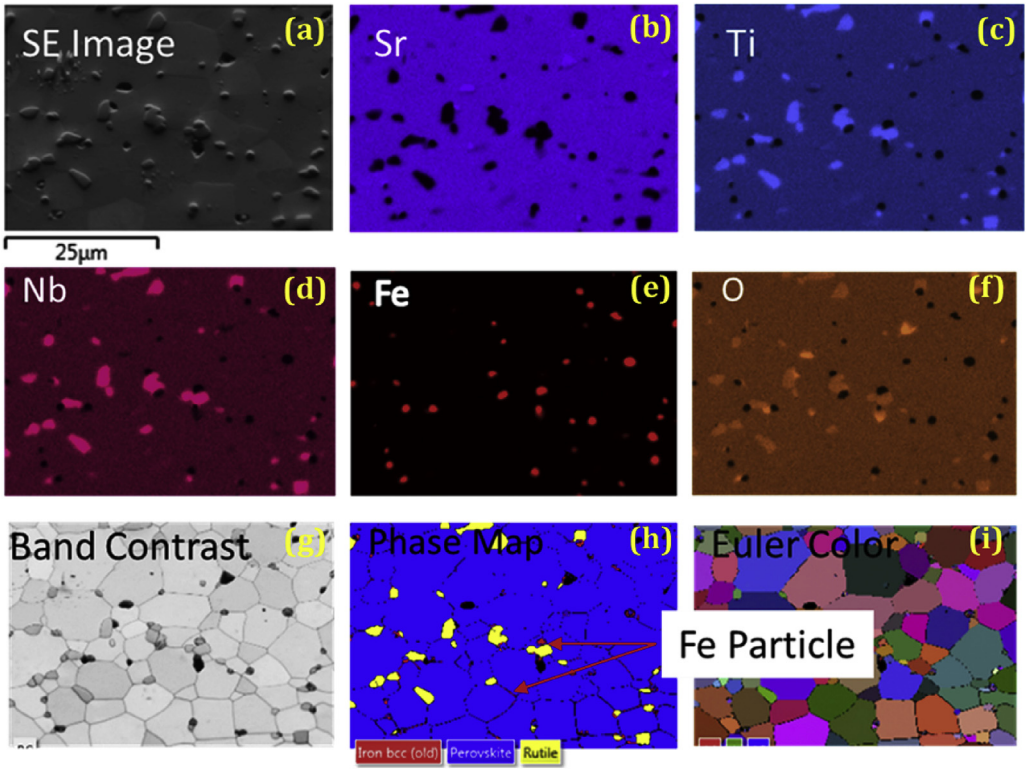

Fig. 3. Micrographs and maps for samples containing Fe: (a) Backscattered electron (SE) image; (b–f) Elemental maps:(b) Sr, (c) Ti, (d) Nb, (e) Fe, (f) O; (g–i) EBSD maps:(g) Band contrast map with grain boundaries showing sharp contrast, (h) Phase distribution map of Fe particles (red) and rutile based phase (yellow) in the $Sr_{0.8}La_{0.06}Ti_{0.8}Nb_{0.2}O_3$ primary phase, (i) Euler false colour maps indicating random orientation of primary phase grains. (For interpretation of the references to colour in this figure legend, the reader is referred to the web version of this article.)

may allow droplets of the partial liquid phase to coalesce at triple point junctions, giving rise to the atypical voids observed in Fig. 2(c).

Interestingly, submicron sized voids in the grains were observed in the samples prepared with Fe additions. Such voids are potential scattering centres for phonons and charge carriers and can significantly reduce the thermal conductivity. EDS/EBSD mapping was carried out on both types of samples prepared with metal additions; data for samples prepared with 2.5% Fe are presented in Fig. 3. The dark phases in Fig. 3 are rich in Ti and Nb (Fig. 3c and d), but deficient in Sr (Fig. 3b). The absence of oxygen at locations where Fe is present (Fig. 3e and f) confirms the location of Fe in metallic, rather than metal oxide form. Whilst the sub-micron inclusions at grain boundaries are only faintly visible in the EDS intensity maps, details of the phase distribution in the microstructure are much more apparent in the band contrast, phase and Euler maps obtained by EBSD (Fig. 3 g–i). The secondary phases are indexed as (i) a rutile based phase, and (ii) a cubic iron phase. The locations of the sub-micron Fe inclusions along grain boundaries are clearly visible in the EBSD generated maps. EDS/EBSD mapping of the Cu-containing samples showed very similar features.

XPS analysis was undertaken to assess the degree of reduction of Ti and Nb in the various samples and the oxidation states of the metallic inclusions. The ratios of Ti^{3+} and Nb^{4+} compared to Ti^{4+} and Nb^{5+} were estimated by de-convoluting the characteristic peaks and determining relevant peak areas. Preliminary XPS investigation of the control (L2) sample sintered under reducing conditions demonstrated that both Ti and Nb had been reduced, with Ti^{3+}/total Ti, and Nb^{4+}/total Nb approximately equal to $10 \pm 2\%$ [19]. The results of XPS analysis of the Cu and Fe containing samples are shown in Fig. 4. Calibration was performed using standard C 1s peak at 284.8 eV; standard peak positions for Cu were taken from NIST database. The Cu 2p3/2 peak position of 932.7 eV is consistent with a Cu oxidation state of zero [46]. However, the spectral lines from Cu (+1), Cu (+2) are very close to Cu (0), necessitating careful calibration. The fitted peak and the Cu-Auger peaks at 570.2 eV

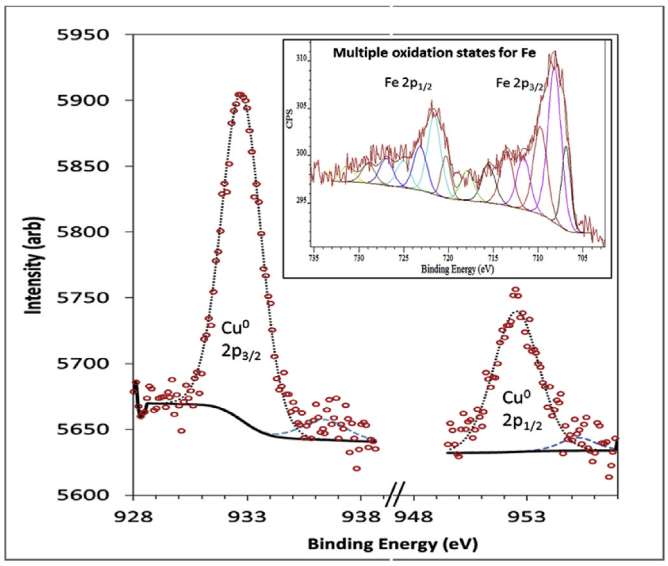

Fig. 4. XPS characteristic peaks for Cu 2p for $Sr_{0.8}La_{0.06}Ti_{0.8}Nb_{0.2}O_3$ sample containing Cu particles; inset shows the existence of multiple oxidation states for Fe 2p in the $Sr_{0.8}La_{0.06}Ti_{0.8}Nb_{0.2}O_3$ sample containing Fe particles.

have higher FWHM (fixed width half maxima) than the reported peak profile data [47]. This suggests surface oxidation of the sample; XPS characterization of Cu (Fig. 4) is consistent with the presence of mixed oxidation states of Cu (0) and Cu (+1) [47].

In contrast, the XPS data for the sample containing Fe particles (Fig. 4 inset) is much more complex, with a strong suggestion of multiple valences of Fe. It is not clear whether the data are representative of the bulk sample; it is known that Fe is more susceptible to oxidation than Cu [48] and has been shown to oxidise readily during XPS experiments [49]. However, for the Fe is plausible that there is gradation in the oxidation states, from Fe^0 in the core of the particle to Fe^{2+}, Fe^{3+} at the contact with $SrTiO_3$. Furthermore it is proposed that the mixed valences are observed for Fe in particular as it is more electropositive than Cu. The Fe-containing sample also showed the presence of the Fe (0) 2p3/2 peak at 707.0 eV and the corresponding Fe (0) 2p1/2 peak at 720.1 eV. Samples with mixed Fe oxidation states frequently display multiple sets of 2p3/2 peaks corresponding to a range of oxidation states (0–4) as shown by Biesinger et al. [50]. Here a typical Gaussian (70%)-Lorentzian (30%) peak has been used to fit the pattern obtained that corresponds to the characteristic signal for Fe oxidation states. The deconvolution of the Fe XPS data into multiple peak sets (inset of Fig. 4) confirms partial oxidation for Fe and the presence of other oxidation states in addition to the elemental form.

The thermoelectric properties of three types of samples are presented in Fig. 5. Repeated measurements on the samples, up to 6 months apart, show less than 5% change, close to the uncertainty in the measurements. Data for La doped single crystal $SrTiO_3$ [51] are included for comparison. The variation of electrical resistivity with temperature (Fig. 5a) suggests that inclusion of Fe/Cu particles within the bulk material does not significantly affect the semiconductor-metallic transition temperature, which occurred at 450 K for all the samples. However, the presence of Fe and Cu particles in the ceramics reduced the bulk electrical resistivity by at least a factor of five, and was well below that of the single crystal data [51]. In fact, samples prepared with Cu additions were at least 40% more conductive than the sample prepared with Fe additions, even though the former samples were less dense. The lowest electrical resistivity obtained for the Cu containing sample was 7.4×10^{-6} Ωm at 500 K. EBSD mapping of the samples suggests the majority of the Fe/Cu is present as inclusions, which range from nanoscale to a few microns in size, and are located along the grain boundaries. EDS analysis of the primary phase grains indicated that less than 0.5 at% Fe or Cu may have diffused into the crystal lattice. Thus reduced electrical resistivity in the samples containing Fe/Cu inclusions probably arises because of additional free electrons provided by the metallic particles, change in carrier concentrations and lowering of grain boundary resistance.

The Seebeck coefficient of the samples increased with increasing temperature (Fig. 5b) confirming n-type behaviour. The values are broadly similar to data reported by Kovalesky et al. [10] for La doped $SrTiO_3$ ceramics, but as anticipated much lower than for single crystal $SrTiO_3$ [51]. The Seebeck coefficients for the present samples containing Fe and Cu particles were significantly lower than for the L2 control samples, with the Cu-containing samples exhibiting the lowest Seebeck values. This reduction in the Fe/Cu-containing samples is attributed to higher carrier concentrations compared to L2 control samples; supporting data are presented below.

The thermoelectric power factor (S^2/ρ) can be calculated from the electrical resistivity and Seebeck data (Fig. 5a and b). The L2 control sample exhibited a maximum power factor at 700 K of 0.8×10^{-3} W/m.K^2. At temperatures less than 400 K the power factor values for samples containing Fe and Cu inclusions were comparable to those for the control sample, while at higher temperatures the power factors for metal containing samples were up to 75% higher. The maximum value for the Cu-containing sample was 1.45×10^{-3} W/m.K^2 at 700 K and the maximum value for the Fe-containing sample was 1.20×10^{-3} W/m.K^2 at 875 K. This improvement for $SrTiO_3$-based samples is comparable to that reported by Dehkordi et al. [9] for Pr-doped $SrTiO_3$ as a result of Pr segregation to the grain boundaries.

3.1. Carrier concentrations

The carrier concentrations for the three types of samples were determined experimentally using a Quantum Design PPMS system, and calculated independently from the Seebeck coefficients [52]. The results are summarised in Table 1. The carrier concentrations were significantly higher in the Cu/Fe containing samples compared to the L2 reference samples. This is directly related to the lower electrical resistivity of the metal-containing samples. It is noted that the Fe-containing samples exhibited higher Seebeck coefficients than the Cu-containing samples, and the latter have a smaller carrier concentrations (Table 1). This is related to the reduced charge mobility and higher m^*/m_0 value (where m^* is the effective carrier mass while m_0 is the rest mass of the charge carriers) for the Fe-containing samples (Table 1). Furthermore, for the Cu-containing sample, the charge mobility was almost doubled compared to the L2 control sample (Table 1). It is proposed that improved carrier properties and simultaneous increased charge mobility helped to increase the power factor for the Cu-containing sample to 1.45×10^{-3} W/m.K^2 at 700 K, whereas reduced mobility led to an increase in electrical resistivity of the Fe-containing sample despite a higher carrier concentration. The difference between the effects of the two metallic inclusions can be attributed to differences in their melting points and their solubilities in the base composition. The presence of a significant liquid phase in the copper containing samples during sintering can give rise to a more uniform distribution of Cu particles along the grain boundaries enhancing conduction, whereas the iron particles are not as well distributed. Iron is much more easily accommodated into the lattice which will enhance the electrical conductivity, although Fe has been shown to associate with oxygen vacancies which can reduce electrical conductivity at the measurement temperatures [53].

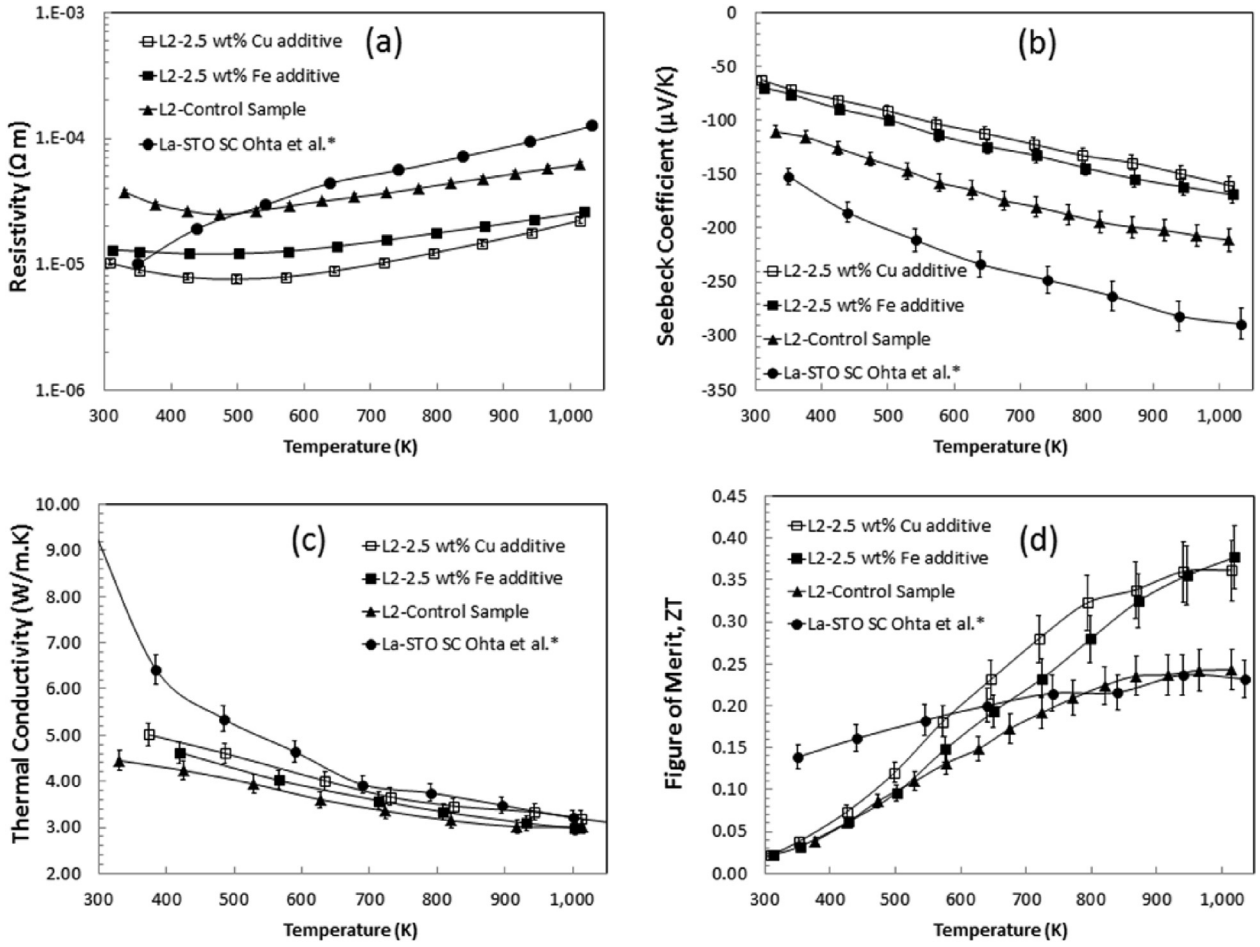

Fig. 5. Thermoelectric properties of the $Sr_{0.8}La_{0.06}Ti_{0.8}Nb_{0.2}O_3$ (control) and the Cu-containing and Fe-containing samples as a function of temperature: (a) electrical resistivity, (b) Seebeck coefficient, (c) thermal conductivity, (d) figure of merit, ZT. Data for doped single crystal $SrTiO_3$ (round solid symbols; taken from Ohta et al. [51] are included for comparison.

Table 1
Carrier concentration, mobility and carrier mass for the three types of samples.

Sample	Carrier concentration (cm^{-3})		Charge mobility $cm^2\ V^{-1}\ s^{-1}$	$\frac{m^*}{m_0}$	$\frac{m^*}{n^{\frac{2}{3}}m_0}$ $10^{-14}\ cm^2$
	Calculated	Measured			
L2	2.0×10^{21}	1.7×10^{21}	1.34	4.3	2.98
L2-Cu	4.6×10^{21}	3.3×10^{21}	2.35	4.21	1.92
L2-Fe	4.2×10^{21}	5.6×10^{21}	0.9	6.71	2.12

3.2. Thermal conductivity

The presence of metallic particles in the $SrTiO_3$ matrix had detrimental effect on thermal conductivity of samples at lower temperatures (Fig. 5c), but was no worse than the single crystal data [51]. The overall thermal conductivity of metallic inclusion-containing samples was typically 10% higher than for the L2 control samples at temperatures below 800 K (Fig. 5c). At the highest temperatures, the Fe-containing samples exhibited the lowest thermal conductivity values. This is probably due to the presence of a high concentration of voids and other submicron features in the samples (Fig. 2b), acting as phonon scattering centres. In contrast, the microstructures of the Cu-containing samples did not display the same level of sub-grain features (Fig. 2c), and therefore the thermal conductivity did not show a comparable level of reduction. Furthermore, the Cu-containing samples were of lower density than the control samples, and that may have contributed to a slight reduction in thermal conductivity. In fact the current $SrTiO_3$-based samples were not as effective in reducing thermal conductivity at higher temperature as the tungsten doped samples reported by Kovalevsky et al. [15]. The latter were more effective because of the presence of the heavier W atoms, acting as efficient scattering centres. However, Xing et al. [54] reported a significant increase in electrical conductivity with the addition of silver, albeit at higher concentrations.

3.3. Thermoelectric figure of merit

The resulting temperature dependence of the thermoelectric figure of merit (ZT) is shown in Fig. 5d. In comparison with the control samples, the Fe/Cu-containing samples exhibited a marked 50% improvement in ZT. The small increase in thermal conductivity brought about by the presence of the inclusions was not sufficient to reduce the power factor to any degree. Indeed, the effect of reduced electrical resistivity dominated, enabling improved power factor and hence, ZT in samples containing metal inclusions. At temperatures up to 900 K the figure of merit for the Cu-containing samples was higher than for other samples, with a maximum ZT of 0.36. The Fe-containing samples displayed an almost linear dependence of ZT with temperature, with a highest ZT of 0.38 at 1000 K. These values show considerable improvement in the figure

of merit compared to control sample and verifies the benefit of employing small metallic inclusions in perovskite thermoelectric ceramics. Once realistic uncertainties in ZT are taken into account (at least ±10%) the highest values here (0.38) are comparable with many of the best values reported for $SrTiO_3$-based ceramics using alternative approaches. For example, Lin et al. [24] achieved a ZT of 0.38 at 1000 K for La doped STO assisted with inclusion of graphene. Zhang et al. [55] reported a ZT of 0.37 at 1000 K for $SrTi_{0.85}Nb_{0.15}O_3$ and Lu et al. [22] obtained a ZT of 0.40 for A-site deficient La doped STO ($La_{0.2}Sr_{0.7}TiO_3$); Dy doping of STO yielded a ZT of 0.41 at 1073 K [10]. Again all these values are within the same significance bands. It is interesting to note that while the ZT values for the ceramics are lower than those for the single crystal data [51] at low temperatures, the ZT values for the ceramics are consistently higher at the higher temperatures.

4. Conclusions

High quality $Sr_{0.8}La_{0.067}Ti_{0.8}Nb_{0.2}O_{3-\delta}$ ceramics containing inclusions of Cu or Fe were prepared under reducing conditions. The presence of Cu led to a slight reduction density to ~94% and reduction in grain sizes to ~ 9–10 μm, whilst Fe enhanced specimen density to 98% theoretical and grain sizes to ~15 μm. The bulk matrix was cubic structured perovskite with space group *Pm-3m*; the metallic inclusions (submicron to micron size) were located along the grain boundaries and there was a rutile-structured minor phase. The Cu inclusions were of valence Cu (0) and Cu (+1), whilst the Fe exhibited multiple valences. Thermoelectric properties were significant improved by the presence of the inclusions. The presence of Fe and Cu reduced the bulk electrical resistivity by at least a factor of 5 and increased the power factor by at least 75%. Although the Seebeck coefficients were reduced, and thermal conductivity slightly increased at low temperatures by the presence of the inclusions, there were important positive effects: the thermal conductivity was reduced at high temperatures and both carrier mobility and carrier concentration increased. The interplay of factors led to a significant increase in the thermoelectric figure of merit from 0.25 at 1000 K for the control sample, to ZT of 0.36 at 900 K for the Cu-containing samples and to 0.38 at 1000 K for the Fe-containing samples.

Acknowledgements

The authors are grateful to the EPSRC for the provision of funding for this work (EP/H043462, EP/I036230/1, EP/L014068/1, EP/L017695/1 acknowledged by RF). All research data supporting this publication are directly available within the publication D. S. acknowledges support through the provision of a President's Scholarship from the University of Manchester.

References

[1] D.M. Rowe, Thermoelectrics Handbook Macro to Nano, CRC Press, Boca Raton, 2006.
[2] F. Kenjiro, M. Tadashi, N. Kazuo, High-temperature thermoelectric properties of $NaxCoO_{2-\delta}$ single crystals, Jpn. J. Appl. Phys. 40 (2001) 4644.
[3] G.K. Ren, J.L. Lan, C.C. Zeng, Y.C. Liu, B. Zhan, S. Butt, Y.H. Lin, C.W. Nan, High performance oxides-based thermoelectric materials, J. Mater. 67 (2015) 211–221.
[4] K. Koumoto, R. Funahashi, E. Guilmeau, Y. Miyazaki, A. Weidenkaff, Y. Wang, C. Wan, Thermoelectric ceramics for energy harvesting, J. Am. Ceram. Soc. 96 (2013) 1–23.
[5] T. Okuda, K. Nakanishi, S. Miyasaka, Y. Tokura, Large thermoelectric response of metallic perovskites $Sr_{1-x}La_xTiO_3$ ($0<x<0.1$), Phys. Rev. B 63 (2001) 113104.
[6] H. Muta, K. Kurosaki, S. Yamanaka, Thermoelectric properties of reduced and La-doped single crystalline $SrTiO_3$, J Alloy Compd 392 (2005) 306–309.
[7] K. Koumoto, Y.F. Wang, R.Z. Zhang, A. Kosuga, R. Funahashi, Oxide thermoelectric materials: a nanostructuring approach, Annu. Rev. Mater. Res. 40 (2010) 363–394.
[8] A.M. Dehkordi, S. Bhattacharya, T. Darroudi, J.W. Graff, U. Schwingenschlogl, H.N. Alshareef, T.M. Tritt, Large thermoelectric power factor in Pr-Doped $SrTiO_{3-\delta}$ ceramics via grain-boundary-induced mobility enhancement, Chem. Mater. 26 (2014) 2478–2485.
[9] A.M. Dehkordi, S. Bhattacharya, J. He, H.N. Alshareef, T.M. Tritt, Significant enhancement in thermoelectric properties of polycrystalline Pr-doped $SrTiO_{3-\delta}$ ceramics originating from nonuniform distribution of Pr dopants, Appl. Phys. Lett. 104 (2014) 193902.
[10] A.V. Kovalevsky, A.A. Yaremchenko, S. Populoh, P. Thiel, D.P. Fagg, A. Weidenkaff, J.R. Frade, Towards a high thermoelectric performance in rare-earth substituted $SrTiO_3$: effects provided by strongly-reducing sintering conditions, Phys. Chem. Chem. Phys. 16 (2014) 26946–26954.
[11] K. Kato, M. Yamamoto, S. Ohta, H. Muta, K. Kurosaki, S. Yamanaka, H. Iwasaki, H. Ohta, K. Koumoto, The effect of Eu substitution on thermoelectric properties of $SrTi_{0.8}Nb_{0.2}O_3$, J. Appl. Phys. 102 (2007) 116107.
[12] H. Muta, K. Kurosaki, S. Yamanaka, Thermoelectric properties of rare earth doped $SrTiO_3$, J Alloy Compd 350 (2003) 292–295.
[13] P. Blennow, A. Hagen, K.K. Hansen, L.R. Wallenberg, M. Mogensen, Defect and electrical transport properties of Nb-doped $SrTiO_3$, Solid State Ionics 179 (2008) 2047–2058.
[14] C. Chen, T.S. Zhang, R. Donelson, T.T. Tan, S. Li, Effects of yttrium substitution and oxygen deficiency on the crystal phase, microstructure, and thermoelectric properties of $Sr_{1-1.5x}Y_xTiO_{3-\delta}$ ($0 \leq x \leq 0.15$), J Alloy Compd 629 (2015) 49–54.
[15] A.V. Kovalevsky, S. Populoh, S.G. Patricio, P. Thiel, M.C. Ferro, D.P. Fagg, J.R. Frade, A. Weidenkaff, Design of $SrTiO_3$-based thermoelectrics by tungsten substitution, J. Phys. Chem. C 119 (2015) 4466–4478.
[16] J. Liu, C.L. Wang, H. Peng, W.B. Su, H.C. Wang, J.C. Li, J.L. Zhang, L.M. Mei, J. Elect. Mater. 41 (2012) 3073–3076.
[17] W.H. Gong, H. Yun, Y.B. Ning, J.E. Greedan, W.R. Datars, C.V. Stager, Oxygen-deficient $SrTiO_{3-x}$, $x = 0.28, 0.17$, and 0.08. Crystal growth, crystal structure, magnetic, and transport properties, J. Solid State Chem. 90 (1991) 320–330.
[18] J. Liu, C.L. Wang, W.B. Su, H.C. Wang, P. Zheng, J.C. Li, J.L. Zhang, L.M. Mei, Enhancement of thermoelectric efficiency in oxygen-deficient $Sr_{1-x}La_xTiO_{3-\delta}Sr_{1-x}La_xTiO_{3-\delta}$ ceramics, Appl. Phys. Lett. 95 (2009) 162110.
[19] D. Srivastava, C. Norman, F. Azough, M.C. Schäfer, E. Guilmeau, D. Kepaptsoglou, Q.M. Ramasse, G. Nicotra, R. Freer, Tuning the thermoelectric properties of A-site deficient $SrTiO_3$ ceramics by vacancies and carrier concentration, Phys. Chem. Chem. Phys. 18 (2016) 26475–26486.
[20] S.R. Popuri, A.J.M. Scott, R.A. Downie, M.A. Hall, E. Suard, R. Decourt, M. Pollet, J.W.G. Bos, Glass-like thermal conductivity in $SrTiO_3$ thermoelectrics induced by A-site vacancies, RSC Adv. 4 (2014) 33720–33723.
[21] A.V. Kovalevsky, A.A. Yaremchenko, S. Populoh, A. Weidenkaff, J.R. Frade, Effect of a-site cation deficiency on the thermoelectric performance of donor-substituted strontium titanate, J. Phys. Chem. C 118 (2014) 4596–4606.
[22] Z.L. Lu, H.R. Zhang, W. Lei, D.C. Sinclair, I.M. Reaney, High-Figure-of-Merit thermoelectric La-Doped a-site-deficient $SrTiO_3$ ceramics, Chem. Mater. 28 (2016) 925–935.
[23] D. Srivastava, F. Azough, M. Molinari, S.C. Parker, R. Freer, High-temperature thermoelectric properties of (1-x) $SrTiO_3$ - (x) $La_{1/3}NbO_3$ ceramic solid solution, J. Elect. Mater. 44 (2015) 1803–1808.
[24] Y. Lin, C. Norman, D. Srivastava, F. Azough, L. Wang, M. Robbins, K. Simpson, R. Freer, I.A. Kinloch, Thermoelectric power generation from lanthanum strontium titanium oxide at room temperature through the addition of graphene, ACS Appl. Mater. Interfaces 7 (2015) 15898–15908.
[25] L.I. Hanbo, Z. Ganhong, D.A.I. Zhenxiang, Y. Zhenheng, W. Haiqiu, M.A. Yongqing, Thermoelectric properties of $Sr_{0.9}La_{0.1}TiO_3$ and $Sr_{2.7}La_{0.3}Ti_2O_7$ with 15% Ag addition, J. Rare Earths 32 (2014) 314–319.
[26] G.H. Zheng, Z.X. Dai, H.B. Li, H.Q. Wang, Y.Q. Li, X.F. Xu, B.T. Wang, Y.Q. Ma, G. Li, Improving the thermoelectric properties of $Sr_{0.9}La_{0.1}TiO_3$ by Ag addition, J. Low Temp. Phys. 174 (2014) 128–135.
[27] Y. Wang, Y. Sui, J. Cheng, X. Wang, W. Su, Comparison of the high temperature thermoelectric properties for Ag-Doped and Ag-Added $Ca_3Co_4O_9$, J. Alloy. Comp. 477 (2009) 817–821.
[28] M. Mikami, N. Ando, R. Funahashi, The effect of Ag addition on electrical properties of the thermoelectric compound $Ca_3Co_4O_9$, J. Solid State Chem. 178 (2005) 2186–2190.
[29] S. Panteny, C.R. Bowen, R. Stevens, Characterisation of barium titanate-silver composites, part I: microstructure and mechanical properties, J. Mater. Sci. 41 (2006) 3837–3843.
[30] S. Panteny, C.R. Bowen, R. Stevens, Characterisation of barium titanate-silver composites part II: electrical properties, J. Mater. Sci. 41 (2006) 3845–3851.
[31] N. Iwagami, H. Nagata, I. Sakaguchi, T. Takenaka, Diffusion behavior of Ag electrodes into $(Bi_{1/2}Na_{1/2})TiO_3$ ceramics, J. Ceram. Soc. Jpn. 124 (2016) 644–647.
[32] M.J. Qin, F. Gao, M. Wang, C.C. Zhang, Q.Q. Zhang, L. Wang, Fabrication and high-temperature thermoelectric properties of Ti-doped $Sr_{0.9}La_{0.1}TiO_3$ ceramics, Ceram. Int. 42 (2016) 16644–16649.
[33] H.-S. Kim, L. Bi, G.F. Dionne, C.A. Ross, Magnetic and magneto-optical properties of Fe-doped $SrTiO_3$ films, Appl. Phys. Lett. 93 (2008) 092506.
[34] K.R. Tolod, C.J.E. Bajamundi, R.L. de Leon, P. Sreearunothai, R. Khunphonoi, N. Grisdanurak, Visible light-driven photocatalytic hydrogen production using Cu-doped $SrTiO_3$, Energy Sources, Part A Recovery, Util. Environ. Eff. 38 (2016) 286–294.
[35] S.J. Litzelman, A. Rothschild, H.L. Tuller, The electrical properties and stability

of SrTi(0.65)Fe(0.35)O(3-delta) thin films for automotive oxygen sensor applications, Sensor. Actuator. B Chem. 108 (2005) 231–237.
[36] S. Steinsvik, R. Bugge, J.O.N. GjØNnes, J. TaftØ, T. Norby, The defect structure of $SrTi_{1-x}Fe_xO_{3-y}$ (x = 0–0.8) investigated by electrical conductivity measurements and electron energy loss spectroscopy (EELS), J. Phys. Chem. Solid. 58 (1997) 969–976.
[37] V.V. Kharton, A.V. Kovalevsky, A.P. Viskup, J.R. Jurado, F.M. Figueiredo, E.N. Naumovich, J.R. Frade, Transport properties and thermal expansion of $Sr_{0.97}Ti_{1-x}Fe_xO_{3-\delta}$ (x=0.2–0.8), J. Solid State Chem. 156 (2001) 437–444.
[38] V.C. Coletta, F.C.F. Marcos, F.G.E. Nogueira, M.I.B. Bernardi, A. Michalowicz, R.V. Gonçalves, E.M. Assafb, V.R. Mastelaro, In situ study of copper reduction in $SrTi_{1-x}Cu_xO_3$ nanoparticles, Phys. Chem. Chem. Phys. 18 (2016) 2070–2079.
[39] F.E. López-Suárez, S. Parres-Esclapez, A. Bueno-López, M.J. Illán-Gómez, B. Ura, J. Trawczynski, Role of surface and lattice copper species in copper-containing (Mg/Sr)TiO3 perovskite catalysts for soot combustion, Appl. Catal. B Environ. 93 (2009) 82–89.
[40] J. Regalbuto, Catalyst Preparation: Science and Engineering, CRC Press, 2006.
[41] H.M. Rietveld, Line profiles of neutron powder-diffraction peaks for structure refinement, Acta Crystallogr. 22 (1967) 151–152.
[42] R. Taylor, Construction of apparatus for heat pulse thermal-diffusivity measurements from 300-3000K, J. Phys. E Sci. Instrum. 13 (1980) 1193–1199.
[43] R.D. Cowan, Pulse method of measuring thermal diffusivity at high temperatures, J. Appl. Phys. 34 (1963) 926–930.
[44] T. Miruszewski, P. Gdaniec, J. Karczewski, B. Bochentyn, K. Szaniawska, P. Kupracz, M. Prześniak-Welenc, B. Kusz, Synthesis and structural properties of (Y, Sr)(Ti, Fe, Nb)$O_{3-\delta}$ perovskite nanoparticles fabricated by modified polymer precursor method, Solid State Sci. 59 (2016) 1–6.
[45] W. Rheinheimer, M. Baurer, M.J. Hoffmann, A reversible wetting transition in strontium titanate and its influence on grain growth and the grain boundary mobility, Acta Mater. 101 (2015) 80–89.
[46] R.J. Bird, P. Swift, Energy calibration in electron spectroscopy and the redetermination of some reference electron binding energies, J. Electron. Spectrosc. 21 (1980) 227–240.
[47] M.C. Biesinger, L.W.M. Lau, A.R. Gerson, R.S.C. Smart, Resolving surface chemical states in XPS analysis of first row transition metals, oxides and hydroxides: Sc, Ti, V, Cu and Zn, Appl. Surf. Sci. 257 (2010) 887–898.
[48] F.A. Cotton, G. Wilkinson, C.A. Murillo, M. Bochmann, R. Grimes, Advanced Inorganic Chemistry, Wiley New York, 1999.
[49] A.P. Grosvenor, B.A. Kobe, N.S. McIntyre, Examination of the oxidation of iron by oxygen using X-ray photoelectron spectroscopy and QUASES, Surf. Sci. 565 (2004) 151–162.
[50] M.C. Biesinger, B.P. Payne, A.P. Grosvenor, L.W.M. Lau, A.R. Gerson, R.S. Smart, Resolving surface chemical states in XPS analysis of first row transition metals, oxides and hydroxides: Cr, Mn, Fe, Co and Ni, Appl. Surf. Sci. 257 (2011) 2717–2730.
[51] S. Ohta, T. Nomura, H. Ohta, K. Koumoto, High-temperature carrier transport and thermoelectric properties of heavily La- or Nb-doped SrTiO3 single crystals, J. Appl. Phys. 97 (2005), 034106.
[52] H. Taguchi, M. Sonoda, M. Nagao, Relationship between angles for Mn–O–Mn and electrical properties of orthorhombic perovskite-type $(Ca_{1-x}Sr_x)MnO_3$, J Solid State Chemistry 137 (1998) 82–86.
[53] S. Andersson, B. Collen, U. Kuylenstierna, A. Magneli, Phase analysis studies on the titanium-oxygen system, Acta Chem. Scand. 11 (1957) 1641–1652.
[54] J. Xing, M. Radovic, A. Muliana, Thermal properties of BaTiO3/Ag composites at different temperatures, Compos. B Eng. 90 (2016) 287–301.
[55] B. Zhang, J. Wang, T. Zou, S. Zhang, X. Yaer, N. Ding, C. Liu, L. Miao, Y. Li, Y. Wu, High thermoelectric performance of Nb-doped $SrTiO_3$ bulk materials with different doping levels, J. Mater. Chem. C 3 (2015) 11406–11411.